PERFORMANCE ANALYSIS AND OPTIMIZATION OF LEAD-FREE TIN-BASED $MASnBr_3$ TANDEM PEROVSKITE SOLAR CELL

Shreyus Goutham Kumar[1], Eshwar A R[2], Tadi Surya Teja Reddy[3], Prashanth C R[4], Gajanan V Honnavar[5]

Article History: **Received:** 27.05.2023 **Revised:** 10.06.2023 **Accepted:** 31.07.2023

Abstract:

This paper presents a study on the simulation of a tandem solar cell using SCAPS 1D software. The tandem solar cell consists of a bottom cell made of crystalline silicon and a top cell consisting of a perovskite solar cell based on $MASnBr_3$. The aim of this study is to evaluate the performance potential of this tandem cell configuration. Simulation results reveal that the tandem cell can achieve a power conversion efficiency of 42.7%, which is higher than that of individual cells. The impact of materials in the hole transport layers (HTLs) and electron transport layers (ETLs) of perovskite solar cells on their PCE are discussed in detail. According to our findings, $CuSbS_2$ and AZO are the best-suited materials for HTL and ETL, respectively. The research also explores the impact of various parameters, including the thickness, bandgap, defect density of the perovskite layer, effect of thickness of ETL and HTL on the performance of the tandem solar cell. The standalone top cell gives an Efficiency (eta) of 30.88% (FF=84.87%, Jsc= 32.02 mA/cm^2, Voc=1.13 V). The standalone bottom cell gives an Efficiency (eta) of 21.80% (FF=85.24%, Jsc=20.30 mA/cm^2, Voc=0.74 v). A TSC with $MASnBr_3$ on c-Si shows an Efficiency of 42.70% (FF=85.24% , Jsc=15.48 mA/cm^2, Voc=1.87 V). Overall, this study underscores the potential of tandem solar cells for efficient photovoltaic energy conversion.

Keywords: Perovskite, Crystalline silicon, tandem solar-cell, numerical simulation, material optimization, SCAPS 1D.

[1]Dept. of Electronics and Communication, PES University, EC Campus, Hosur Road, Near Electronic City, Bangalore 560100, India and Research Scholar in Dept on ETE, Dr. AIT, Affiliated to VTU, Belagavi, India.

[2,3]Dept. of Electronics and Communication, PES University, EC Campus, Hosur Road, Near Electronic City, Bangalore 560100, India

[4]Dept. of Electronics and Telecommunication, Dr. Ambedkar Institute of Technology, Affiliated to VTU, Bengaluru, Karnataka 560056, India

[5]Dept. of Science and Humanities, PES University, EC Campus, Hosur Road, Near Electronic City, Bangalore 560100, India

DOI: 10.31838/ecb/2023.12.6.251

1. Introduction

Energy demand has risen dramatically in the preceding century [1]. In the following few decades, its miles predicted that this demand may be doubled. The main source of energy that is used now is fossil fuels, which have a horrible impact on the surroundings and lead to worldwide warming. Clean Energy devices are promising for the industrial marketplace, especially photovoltaics, because of their benefits of providing clean energy, converting daylight into electricity without pollutants, and running for a long term without any preservation. Due to this, plenty of effort changed into placed into growing state-of-the-art photovoltaic technology to lower processing charges and increase conversion performance.

Halide perovskites are a group of materials which have proven capacity for overall high performance and low manufacturing prices in the solar cell [2], [3]. The name "perovskite" comes from the nickname for the crystal shape, despite the fact that other styles of non-halide perovskites (consisting of oxides and nitrides) are utilized in different electricity technology, inclusive of gas cells and catalysts. Perovskite solar cells have become highly effective in an extremely brief time, but there are numerous challenges that stay before they have the ability to become a competitive commercial technology.

Perovskite solar cells with inorganic halides, for example, Sb, Ag, Sn, Cu, Ge and Bi created solar cells, were explored as potential lead substitutes [4]–[7]. A Perovskite containing metal halide, $CH_3NH_3SnBr_3$ has already been regarded as a conceivable option for non-lead PSCs because of its perfect band gap of 1.3 eV [8], [9].

The core part of a solar cell is pure silicon, which has already been utilized as an electrical component for decades. Silicon solar cells are repeatedly referred to as '1st generation' cells as they gained ground already in the 1950s at present, over 90% of the common solar cell market is as dependent on silicon. In comparison with other PV materials, Crystalline silicon(c-Si) with an energy bandgap of 1.12eV is amongst the most necessary candidates for creating multijunction cells due to its proper bandgap, elevated efficiency, price competitiveness, non-toxicity and excellent stability. Nowadays, the various types of crystalline silicon (Si) solar cells dominate the market of photovoltaics. More than 25 % performance can be accomplished by means of silicon solar cells [10].

Tandem Solar devices are traditionally assembled either over mechanical stacking or over a monolithic procedure. Mechanically stacked devices are manufactured by assembling discrete layers on top of one another with the highest band gap material on the top. A monolithic configuration, on the contrary, is composed of numerous absorber layers grown on a substrate. Such a form is more complicated than easy mechanical stacking since, for a delivered spectral distribution, the absorber thickness needs to be adapted to produce similar currents. Each monolithic and mechanically stacked Si-perovskite tandem devices are a commercially feasible technology in 2020, with devices boasting efficiencies of more than 30% [11]. They have the ability to react to many distinct wavelengths of light, which allows them to transform more of the sunlight that arrives at them into electricity. Furthermore, they provide resilience, semi- transparency, tailor-made beget factors, lightweight and more. Countless TSC configurations were thoroughly investigated to triumph over the Shockley – Queisser power conversion efficiency (PCE) restriction of 31% for single-junction cells [12].

The simulations of the devices are dependent on the solar cell's one – dimensional form. SCAPS (a Solar Cell Capacitance Simulator) is a one- dimensional solar cell simulation programme developed at the Department of Electronics and Information Systems (ELIS) of the University of Gent, Belgium [13]. It was originally developed for polycrystalline cell structures of the CuInSe2 and the CdTe family. It is designed to accommodate thin films, multiple interfaces, and large band gaps (Eg=1.12eV for Si, but 2.4eV for CdS used as a window layer). The package evolved over the years to include additional mechanisms, e.g., Auger recombination, tunnelling, multiple enhancement to the user interface, etc.

So here in this paper, we are going to look at the Simulation of tandem lead - free organic–inorganic hybrid PSC ($MASnBr_3$) with

traditional silicon solar cell (crystalline silicon (c-Si)) using SCAPS - 1D.

2. Materials and Methodology

A. Structure of the device and input data

While simulating the tandem PSC the top cell and bottom cell are simulated separately first. The tandem structure consists of a Perovskite solar cell with $MASnBr_3$ perovskite as the top sub cell and traditional crystalline silicon (c-Si) is the bottom sub cell.Fig. 1. depicts the composition of a reference Perovskite Solar Cell that was initially simulated in this study. In this structure, the absorber layer is taken as methylammonium tin bromide (MASnBr3), the transparent conducting oxide used is a fluorine-doped tin oxide (FTO or SnO2: F) and gold (Au) is taken for the back contact.

Fig. 1. Design of the non-lead PSC.

To begin with, Spiro-OMeTAD and TiO_2 are taken as the Hole Transport Material and Electron Transport Material respectively. In the later section, we test the perovskite layer with different ETL and HTL materials and select the best material which maximizes the cell performance. All physical and electrical parameters that are needed for the above selected materials are got from the foregoing theoretical and experimental analysis [14]–[17] and they are shown in Table I. We must study the interface layers as they play a crucial role in the capture of electrons and holes, hence two interface layers are inserted in the PSC. One interface layer is placed between the ETL and the MASnBr3 absorber (ETL/perovskite interface) (IL1) and the other one is placed among the absorber layer and the HTL (perovskite/HTL interface) (IL2). The defect type and the energy distribution for the perovskite layer are set as neutral and Gaussian distribution respectively, and the characteristic energy is taken as 0.1 eV with energy greater than the valence band of 0.6 eV [9]. The defects in the two interface layers are set as neutral single defects, having an energy of 0.6 eV above the valence band. In this work, device modelling and simulation have been performed on solar cell capacitance simulator-one dimension (SCAPS-1D) using AM1.5 Global solar illumination spectrum along with an incident power density of 1000 W/m^2 and at a temperature of 300 K. The simulation results of the reference cell are got as Voc = 0.91 V, Jsc = 32.38 mA/cm^2, FF = 78.98% and PCE = 23.30%.

Table I Input Parameters for Reference Perovskite Solar Cell

Parameters	**FTO**	**TiO_2**	**$MASnBr_3$**	**Spiro-OMeTAD**
Thickness (nm)	500	100	500	200
E_g (eV)	3.5	3.2	1.3	3.0
χ (eV)	4.0	3.9	4.170	2.45
ϵ_r	9.0	9.0	10	3.0
N_c (cm^{-3})	$1x10^{19}$	$1x10^{21}$	$2.2x10^{18}$	$1x10^{19}$
N_v (cm^{-3})	$1x10^{19}$	$2x10^{20}$	$1.8x10^{18}$	$1x10^{19}$
μ_n (cm^2/Vs)	100	20	1.6	0.0002
μ_p (cm^2/Vs)	25	10	1.6	0.0002
N_d (cm^{-3})	$2x10^{19}$	$1x10^{17}$	$1x10^{13}$	0
N_a (cm^{-3})	0	0	$1x10^{13}$	$1x10^{18}$
N_t (cm^{-3})	$1x10^{14}$	$1x10^{15}$	$1x10^{15}$	$1x10^{15}$

Now to get the best ETL and HTL materials such that the cell functioning is maximized, various ETL materials such as (C_{60}, AZO, $Cd_{0.5}Zn_{0.5}S$, CdS, IGZO, PCBM) whose parameters are got from various published reports [9], [14], [15], [18]–[21] which are summarized in Table II are substituted and the simulation is carried out following the same method as

Table II Properties of different ETL materials above.

Parameters	**C_{60}**	**CdS**	**$Cd_{0.5}Zn_{0.5}S$**	**IGZO**	**PCBM**	**AZO**
E_g (eV)	1.7	2.4	2.8	3.05	2	3.3
χ (eV)	3.9	4.2	3.9	4.16	3.9	3.8
ϵ_r	4.2	10	10	10	3.9	9
N_c (cm^{-3})	$8\ x10^{19}$	$2.2x10^{18}$	$1x10^{18}$	$5x10^{18}$	$2.5\ x10^{21}$	$4\ x10^{18}$
N_v (cm^{-3})	$8\ x10^{19}$	$1.8x10^{19}$	$1x10^{18}$	$5x10^{18}$	$2.5\ x10^{21}$	$1x10^{19}$
μ_n (cm^2/Vs)	0.08	100	100	15	0.2	100
μ_p (cm^2/Vs)	0.0035	25	25	0.1	0.2	25
N_d (cm^{-3})	$2.6x10^{18}$	$1x10^{17}$	$1x10^{17}$	$1x10^{18}$	$2.93\ x10^{17}$	$1x10^{18}$
N_a (cm^{-3})	0	0	0	0	0	0
N_t (cm^{-3})	$1x10^{14}$	$1x10^{17}$	$1x10^{15}$	$1x10^{15}$	$1x10^{15}$	$1x10^{15}$

Various HTL materials such as (Cu_2O, CuI, PEDOT: PSS, $CuSbS_2$, NiO, and CuSCN) whose parameters are also got from various published reports [14]–[18] which are summarized in Table III are substituted and the simulation is done in the same method as above.

The thickness of different ETL and HTL materials in the PSC are kept at 100 nm and 200 nm respectively to check their results with the PSC having TiO_2 as ETL and Spiro-OMeTAD as HTL.

Table III Properties of different HTL materials

Parameters	**Cu_2O**	**CuI**	**CuSCN**	**NiO**	**PEDOT:PSS**	**$CuSbS_2$**
E_g (eV)	2.17	2.98	3.4	3.8	2.2	1.58
χ (eV)	3.2	2.1	1.9	1.46	2.9	4.2
ϵ_r	6.6	6.5	10	11.7	3	14.6
N_c (cm^{-3})	$2.5x10^{20}$	$2.8x10^{19}$	$1.7x10^{19}$	$2.5x10^{20}$	$2.2\ x10^{15}$	$2x10^{18}$
N_v (cm^{-3})	$2.5\ x10^{20}$	$1x10^{19}$	$2.5x10^{21}$	$2.5x10^{20}$	$1.8\ x10^{18}$	$1x10^{19}$
μ_n (cm^2/Vs)	80	0.00017	0.00015	2.8	0.02	49
μ_p (cm^2/Vs)	80	0.0002	0.1	2.8	0.0002	49
N_d (cm^{-3})	0	0	0	0	0	0
N_a (cm^{-3})	$1x10^{18}$	$1x10^{18}$	$1x10^{18}$	$1x10^{18}$	$3.17x10^{14}$	$1.38x10^{18}$
N_t (cm^{-3})	$1x10^{15}$	$1x10^{15}$	$1x10^{14}$	$1x10^{15}$	$1x10^{15}$	$1x10^{14}$

Then we simulate the bottom cell i.e., crystalline silicon using the transmitted spectrum (sun spectrum filtered by the top cell). This will also be simulated in the same way as the top cell using SCAPS – 1D [22]. The structure of c-Si consists of three layers n+ Si, p Si and p+ Si as shown in Fig 15.

The n+Si layer is a highly doped layer of n-type silicon. This layer is usually created by diffusing phosphorous or arsenic into the surface of the silicon wafer. The n+Si layer serves as the contact layer for the front electrode of the solar cell. This layer has a low resistance and allows electrons to flow easily from the front electrode to the n-type region. The p-type Si layer is a lightly doped layer of p- type silicon. This layer is usually created by diffusing boron into the silicon wafer. The p- type Si layer forms a p-n junction with the n-type Si layer, which is the basis of the solar cell. When light shines on the solar cell, it creates electron-hole pairs in the p-n junction. The electric field in the junction separates these pairs, which generates a voltage across the cell. The p+Si layer is a highly doped layer of p-type silicon that is located at the back of the solar cell. This layer is usually created by diffusing boron into the back surface of the silicon wafer. The p+Si layer serves as the contact layer for the back electrode of the solar cell. This layer has a low resistance and allows holes to flow easily from the back electrode to the p-type region .

B. Numerical Methods

The numerical simulations in this work are performed utilizing the SCAPS program, which is a one-dimensional (1-D) photovoltaic simulator created by ELIS, University of Gent,

Belgium [13]. SCAPS software can successfully simulate many types of photovoltaic materials since it is flexible and includes almost all required electrical, optical, and photovoltaic models. In general, SCAPS 1D solves the four equations given below in Equations 1 to 4 which represent the photovoltaic equations for hole and electron carrier density independently [23].

Poisson equation:

$$\frac{d^2\varphi(x)}{dx^2} = \frac{e}{\epsilon_0\epsilon_r}(\boldsymbol{p(x) - n(x) + N_D - N_A + \rho_p - \rho_n}) \quad (1)$$

Where e is the electronic charge, φ is the electrostatics potential, ε_0 is the permittivity of space, ε_r is t permittivity, N_A is shallow acceptor impurity density and N_D is shallow donor impurity density. Like the electron density distribution, ρ_p is the hole density distribution and the hole and electron densities as of x are denoted by p(x) and n(x), respectively.

Continuity equation:

$$\frac{dJ_n}{dx} = G - R$$
$$\frac{dJ_p}{dx} = G - R \quad (2)$$

Where the current density of the electron is J_n, the current density of the hole is J_p, while the generation and recombination rates are G and R respectively.

Charge transport equation:

$$J_n = D_n\frac{dn}{dx} + \mu_n n\frac{d\varphi}{dx}$$
$$J_p = D_p\frac{dp}{dx} + \mu_p p\frac{d\varphi}{dx} \quad (3)$$

Where the electron mobility is denoted by μ_n, hole mobility is denoted by μ_p, electron diffusion coefficient and hole diffusion coefficients are D_n and D_p respectively.

Absorption coefficient equation:

$$\alpha(\lambda) = \left(A + \frac{B}{h\nu}\right)\sqrt{h\nu - E_g} \quad (4)$$

Where A and B are constants, h is the Plank constant, E_g is the absorber layer's band gap and v is photon frequency.

Transmitted Spectrum:

The filtered spectrum or the transmitted spectrum from the top sub cell to the bottom sub cell is to be calculated to simulate the tandem solar cell. It can be calculated by using the formula [24]:

$$S(\lambda) = S_0.\exp\left(\sum_{i=1}^{4} -\alpha_{mat_i}(\lambda)d_{mat_i}\right) \quad (5)$$

Where S(λ) is the filtered or transmitted spectrum, $S_0(\lambda)$ is the sun spectrum, 'i' is the layer number, α(material) is the absorption coefficient of that particular material, and 'd' is the thickness of the layer in cm.

The absorption coefficient of the material can be calculated by using the formula [24]:

$$\alpha(E) = A_\alpha\sqrt{h\nu - E_g} \quad (6)$$

Where $A_\alpha = 10^5$ $cm^{-1}eV^{-1/2}$ [25], 'h' is the plank's constant in eV.sec, ν is the spectrum frequency in sec^{-1} and E_g is the band gap of the material in eV. The filtered spectrum is shown in Fig 2.

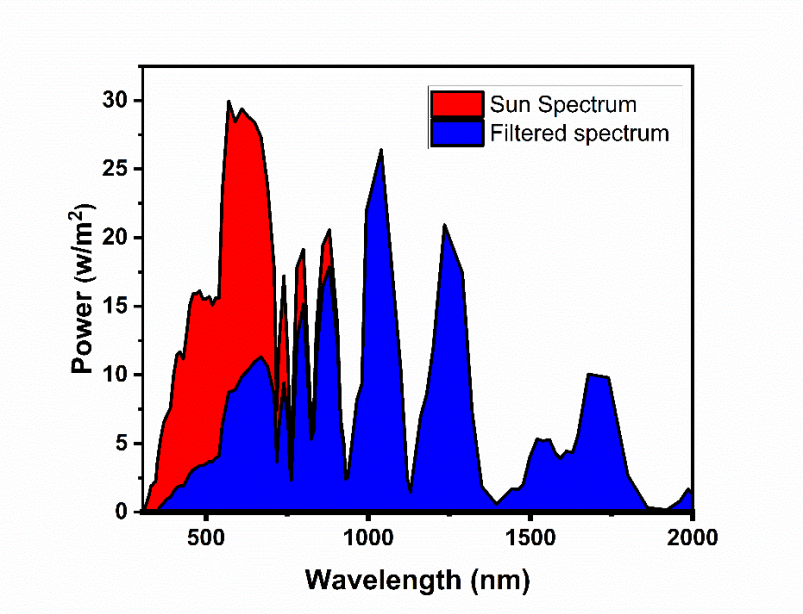

Fig. 2. Sun spectrum and transmitted spectrum

3. Results and Analysis

A. Validation and Simulation

As described in Section II, the construction of the reference perovskite solar cell is depicted in Fig. 1, where Spiro-OMeTAD and TiO_2 are used as HTL and ETL materials, respectively. In the following section, we optimize the reference PSC by selecting appropriate ETL and HTL materials, optimizing the absorber layer thickness, investigating the effect of defect densities in the absorber layer, optimizing the thickness of selected ETL and HTL materials, and finally investigating the effect of the PSC's bandgap. The proposed PSC's structure is seen in Fig. 13. The proposed absorber layer $MASnBr_3$ properties are validated through synthesis and DFT calculations reported in [26]–[28]. Also, the optimum values of the absorber layer fall in the range reported in [26]–[28] which further validates the simulation results.

Table IV Device parameter comparison of $MASnI_3$/$MASnBr_3$ - based PSC with earlier reported outcomes

Device Architecture	J_{SC} (mA/cm^2)	V_{OC} (V)	FF (%)	PCE (%)
FTO/c-TiO_2/mp-TiO_2/ $MASnI_3$/Spiro-OMeTAD/Au [29]	16.8	0.88	42	6.4
FTO/c-TiO_2/ $MASnI_3$/ Spiro-OMeTAD/Au [30]	15.18	0.716	50	5.44
FTO/c-TiO_2/mp-TiO_2/ $MASnI_3$/Au [31]	21.1	0.32	46	3.15
ITO/ZnO/$MASnI_3$/ $CuSbS_2$/Ag [32]	33.19	0.876	76.19	22.16
Glass-base / FTO / $Cd_{0.5}Zn_{0.5}S$ / $MASnI_3$ / $MASnBr_3$ / Au [9]	32.48	0.96	76.40	23.86
FTO/c-TiO_2/mp-TiO_2/ $MASnBr_3$/ Spiro-OMeTAD/Au [33]	8.26	0.88	59	4.27

FTO/c-TiO_2/mp-TiO_2/ $MASnBr_3$/P3HT/Au [34]	4.27	0.50	49	1.12
ITO/PEDOT:PSS/ $MASnBr_3$/ PCBM/Bis-C_{60}/Ag [35]	4.5	0.20	36	0.3
n-TiO_2/i- MASnBr3 /p-NiO [36]	31.88	0.80	84.89	21.66
Glass-base / FTO / AZO / $MASnBr_3$ / $CuSbS_2$ / Au (this work]	**32.02**	**1.13**	**84.87**	**30.88**

Various device architectures with $MASnI_3$ and $MASnBr_3$-based PSC are shown in Table IV. With $MASnI_3$ as the absorber layer, results reported in [29]–[31] are experimental based and it is observed that a maximum PCE of 6.4 is obtained. For the same absorber layer, simulation results are reported in [9], [32] where a PCE of 23.86 is the maximum. Using $MASnBr_3$ as the Perovskite layer in the solar cell, experimentally obtained results show that 4.27 is the maximum PCE [33]–[35]. Whereas in simulation, [36] reports an efficiency of 21.66. With the device architecture of Glass-base / FTO / AZO / MASnBr3 / CuSbS2 / Au in the proposed work, an efficiency of 30.88 is obtained which is the highest when compared to all the reported works.

B. Influence of various ETL materials on the performance of the cell

The simulation results acquired for the perovskite solar cells with different ETL materials are shown in Table II and the reference HTL (Spiro-OMeTAD) is reported in Table V.

Table V Results of PSCs with various ETL materials.

Response	**C_{60}**	**CdS**	**$Cd_{0.5}Zn_{0.5}S$**	**IGZO**	**PCBM**	**AZO**
Voc (V)	0.9131	0.9115	0.9156	0.9148	0.9146	0.9160
Jsc (mA/cm^2)	30.34	32.32	32.36	32.34	32.20	32.38
FF (%)	79.09	78.77	78.69	78.99	78.94	79.05
PCE (%)	21.92	23.21	23.33	23.37	23.25	23.45

The plots of acquired J-V characteristics are shown in Fig. 3. From Table IV we can see that C_{60} when used as ETL in the PSC gives the lowest PCE while AZO produces the highest PCE. Performance of PSC with TiO_2 ETL (the gold standard material) and IGZO ETL is also allowable.

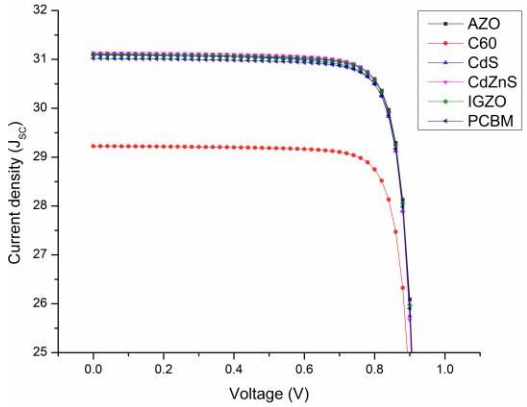

Fig. 3. Plot of J-V characteristics for various ETL materials.

The effect of various ETL materials on the quantum efficiency (QE) of the PSCs are shown in Fig. 4. It is seen that the QE values got for various PSCs are nearly same when the incident wavelength is more than 750 nm. If the wavelength is below 750 nm, the PSC with C_{60} ETL gives the lowest QE of all the QE results, causing inadequate photon absorption. Furthermore, charge collection is limited by C_{60}'s poor electron mobility. When compared to other ETL materials, C_{60} has the lowest J_{SC} and PCE, and should not be utilized to construct lead-free PSCs, according to our simulation.

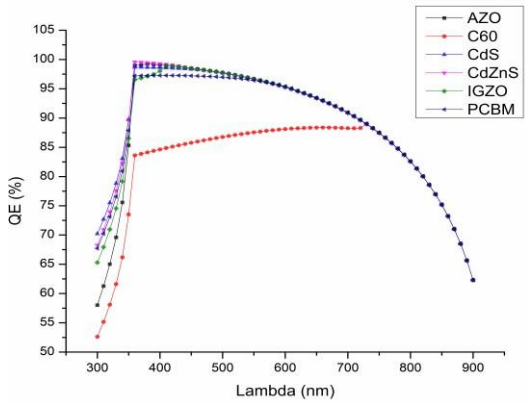

Fig. 4. Plot of QE of PSCs with different ETL materials.

Fig. 5. demonstrates that, except CdS, nearly all ETL materials examined had a greater conduction band (CB) level than the $MASnBr_3$ perovskite. The difference between the ETL and perovskite CB values is known as the conduction band offset (CBO). If the ETL's CB level is lower than the perovskite's, there will be an energy cliff occurring at the ETL/perovskite interface (CBO will be negative). When the CBO is positive, an energy spike will develop otherwise. As a consequence, at the CdS/perovskite contact, an energy cliff occurs, whereas energy spikes form at the interfaces of perovskite and the other ETL materials. The photogenerated electron flow will not be affected by the formation of an energy cliff. But the activation energy needed for carrier recombination (the difference between the band-gap of perovskite and the total value of CBO) decreases as the perovskite's bandgap decreases [37], [38], indicating that interface recombination may take the lead in PSC device recombination. V_{oc} drops as the rate of recombination increases. As a result, as V_{oc} drops, the PCE lowers, and the PCE of the solar cell with CdS as ETL is very low. In the other ETL materials, the photoelectrons will be blocked caused by the development of the energy spike at the ETL/perovskite interface. However, because the activation energy needed for carrier recombination is the same as the bandgap of the perovskite, it is higher than that estimated by the energy cliff, due to which the performance of the cell increases significantly. It's been shown that an energy spike in a limited range has less influence on photo-generated electron motion but a bigger impact on carrier recombination rate [39]. The PSC using AZO as ETL provides a greater PCE because its CB level is higher than that of other ETL materials and its mobility is higher. As a consequence, for the proposed lead-free PSC, AZO is chosen as the optimum ETL material.

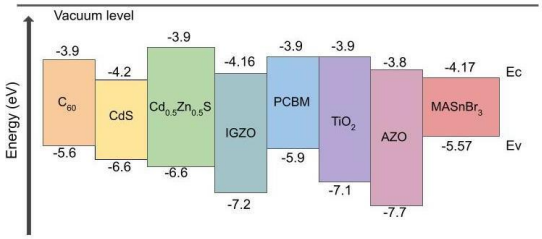

Fig. 5. Band arrangement between different ETL materials and $MASnBr_3$ perovskite.

C. Influence of various HTL materials on the performance of the cell

After selecting the ETL material, various HTL materials used to study the lead-free PSC with AZO as the ETL, listed in Table III are simulated on SCAPS-1D software and the results are plotted in Fig. 5-7. The J-V characteristics got with different HTL materials are shown in Fig. 6.

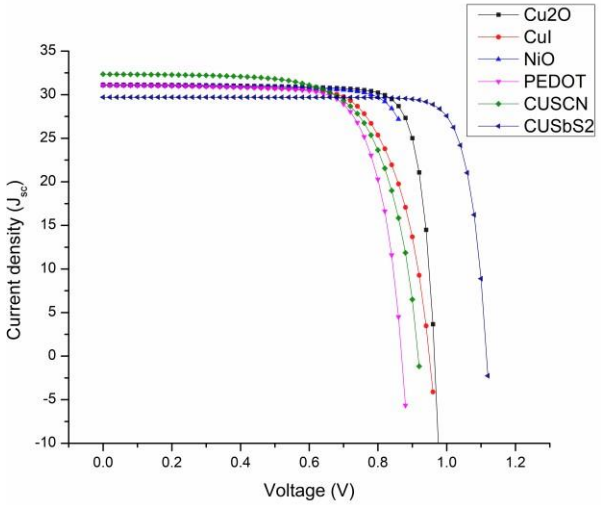

Fig. 6. Plot of J-V characteristics for different HTL materials.

From Fig. 7. we can see that the QE values got with different HTL materials do not vary significantly.

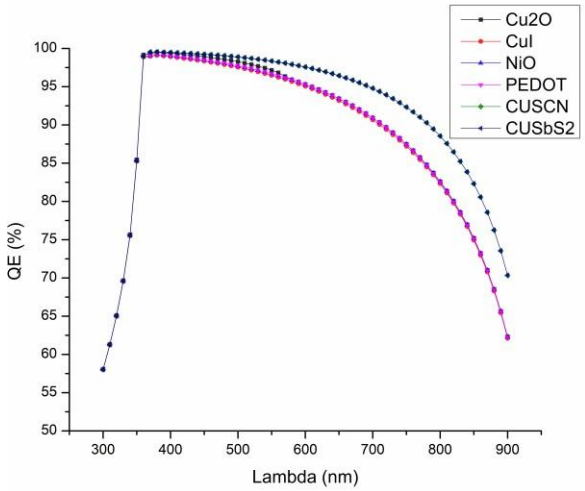

Fig. 7. Plot of QE of PSCs with various HTL materials.

From Table VI we can see that PEDOT: PSS when used as HTL gives the least PCE whereas $CuSbS_2$ HTL gives the maximum PCE.

Table VI Results of PSCs with various HTL materials.

Response	**Cu_2O**	**CuI**	**PEDOT: PSS**	**NiO**	**CuSCN**	**$CuSbS_2$**
Voc (V)	0.9124	0.9066	0.8409	1.1331	0.9173	0.9192
Jsc (mA/cm^2)	32.38	32.31	32.38	32.34	32.34	32.67
FF (%)	77.21	61.54	63.69	57.72	69.58	81.19
PCE (%)	22.82	18.03	17.41	21.16	20.64	24.38

The lower valence band level of $CuSbS_2$ when compared to $MASnBr_3$ material (Fig. 8), causes an energy spike at the perovskite/$CuSbS_2$ interface and hence the activation energy for the carrier recombination is high. Energy cliffs will be developed at the perovskite/HTL interface for other HTL materials as the VB level of those materials is higher than that of the $MASnBr_3$ layer. The photo-generated holes are not obstructed by the energy cliffs, which are similar to the ETL materials. Because of the cliffs, the activation energy for carrier recombination falls below the perovskite's bandgap, increasing interface recombination and lowering cell performance.

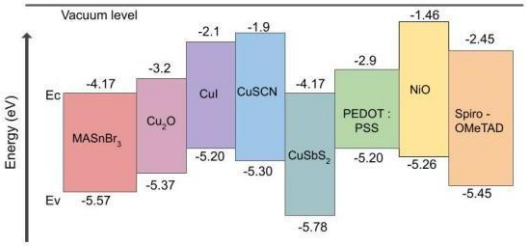

Fig. 8. Band arrangement between different HTL materials and $MASnBr_3$ perovskite.

D. Absorber layer ($MASnBr_3$) thickness optimization

The active perovskite absorber layer has a large impact on the cell's performance. A numerical simulation is also used to look into the importance of the thickness of the perovskite layer upon cell functioning. Fig. 9. shows the effects of changing the thickness from 100 nm to 1000 nm. The figure illustrates that as the absorber layer thickness rises, the J_{sc} and PCE values increase while the V_{oc} and FF values decrease. As the absorber layer thickness rises, more photons are absorbed by the layer, increasing the J_{sc} value. As a result, a rise in J_{sc} is caused by an increase in excess carrier concentration. Contrarily, when the thickness of the absorber layer rises, so does the series resistance value in the solar cell and the internal power depletion, resulting in a constant decline in FF and V_{oc}. The PCE reaches its maximum and begins to drop as the thickness approaches and exceeds 500 nm, as seen in Fig. 9.

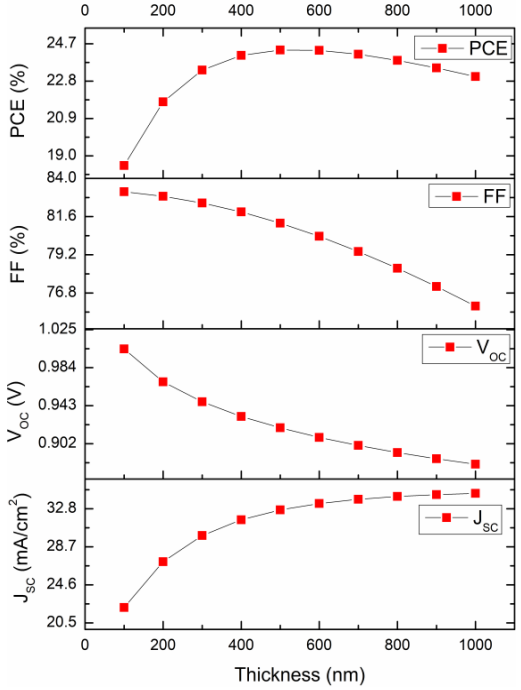

Fig. 9. Influence of Absorber layer thickness on PCE parameters.

PCE can be calculated by Equation 7.

$$PCE = \frac{J_{sc}V_{oc}FF}{P_S} \quad (7)$$

where P_s is the solar irradiation to the Earth. It's simple to calculate PCE for different thicknesses by taking J_{sc}, V_{oc} and FF values from Fig. 9's data and plugging them into Equation (7).

E. Influence of absorber layer ($MASnBr_3$) defect density

The perovskite absorber layer is the primary source of photogenerated electrons. As a result, the features of perovskite absorption sheets have a considerable effect on cell performance. Absorption film quality is strongly influenced by defect density. A perovskite absorber layer having a greater density of defect has a worse standard and a higher carrier recombination rate than a carrier generation rate [40]. The performance of PSCs with varying absorption layer defect densities is simulated in this paper to assess the effect of the density of defects of the absorber layer on the performance of the cell. This study's defect density results range from 10^9 to 10^{13} cm^{-3} [41]. From Fig. 10, it is evident that as the absorber layer defect density rises, the PCE and FF decreases.

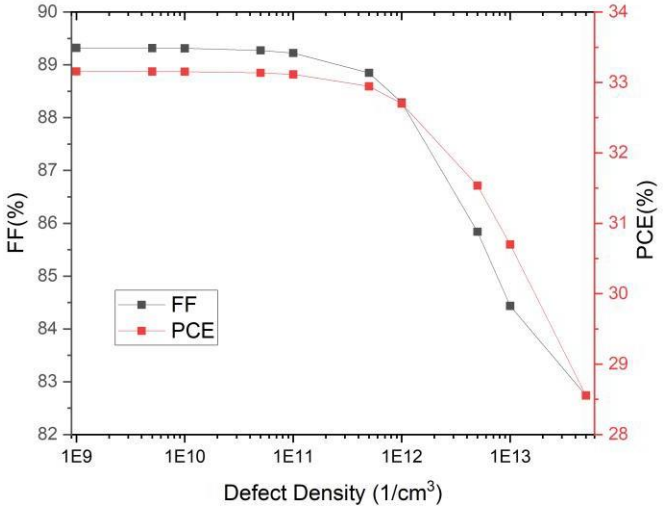

Fig. 10. Plot of absorber layer defect density Vs PCE.

A deep energy level defect serves as a nonradiative Shockley-Read-Hall (SRH) recombination center. As a result, the short minority carrier lifetime reduces as the density of defects in the absorber layer rises, while charge recombination increases, resulting in a drop in V_{oc} and J_{sc}. Moreover, the PSC becomes semi-insulating and the required p-n junction does not develop when the doping density is equivalent to or less than the defect density in the absorber [42], [43], resulting in poor cell performance. As a result, in order to obtain optimal PSC performance, the density of defects in the absorber layer must be reduced or even removed. Moreover, with current manufacturing developments, it is still exceedingly difficult to dramatically decrease defect density. According to our findings, the defect density in the absorber layer should not be greater than 10^{15} cm^{-3} to obtain good cell performance.

F. Optimization of selected ETL (AZO) thickness

The aluminium-doped ZnO (AZO) serves as an ETL for the photovoltaic response, improving it is critical for a good solar cell. The PCE of the proposed solar cell was investigated for thickness optimization by altering the AZO layer thickness from 100 to 1000 nm, and the simulated results are summarized in Fig. 11. From the results, we can finalize that 100 nm (PCE 26.42 percent) is the best suited AZO layer thickness for the proposed solar cell.

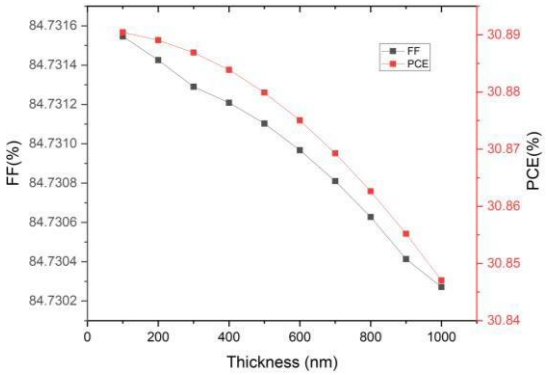

Fig. 11. Effect of ETL thickness on PCE.

G. Optimization of HTL ($CuSbS_2$) thickness

The HTL plays a crucial role in preserving the reacted levels of the $MASnBr_3$ absorber layer and successfully controlling the conduction of holes (carriers). When the thickness of the Hole Transport Layer is too thin, light absorption is reduced, resulting in low efficiency. To study the effect of the thickness of HTL on PCE, the thickness of the $CuSbS_2$ layer is altered from 100 nm to 1000 nm and from the results shown in Fig. 12, we see that an ideal thickness of 400 nm is suitable for high efficiency and fill-factor. Our findings demonstrate that no HTL, as well as a very thin (less than 100 nm) or thick HTL (more than 400 nm), is not acceptable for high efficiency.

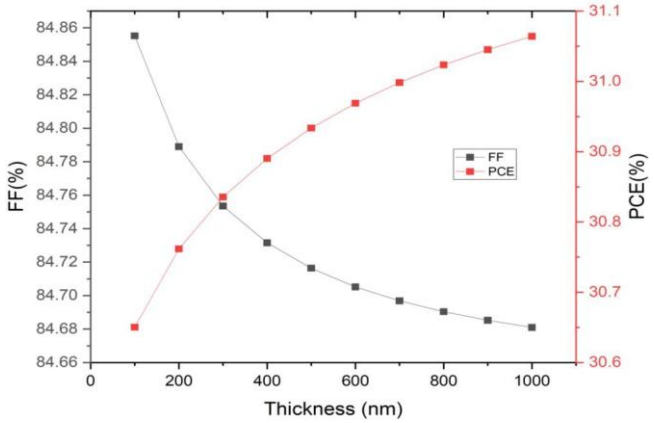

Fig. 12. Effect of HTL thickness on FF.

H. Influence of the Band-Gap of the absorber layer

The Band Gap of $CH_3NH_3SnBr_3$ is in the span of 1.25 eV to 1.5 eV [44] and hence when we alter the band gap of the absorber in this range. From the simulated results plotted in Fig. 13. we see that the optimum band gap for high Efficiency is 1.33 eV. Hence, we fix the band gap of the absorber layer as 1.33 eV. [45]

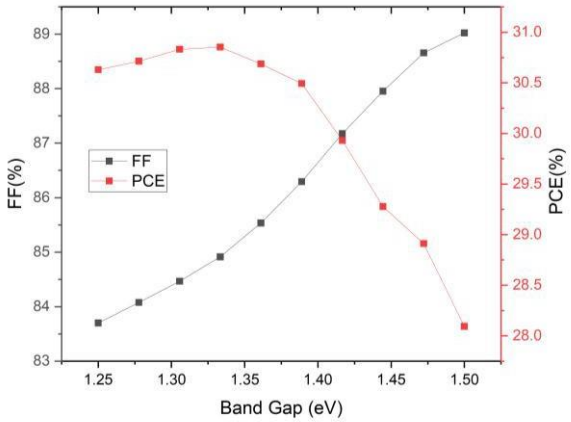

Fig. 13. Effect of band gap on PCE.

Finally, Table VII compares all the parameters ($J_{SC,}$ $V_{OC,}$ FF, PCE) of the reference perovskite solar cell with the proposed perovskite solar cell.

Table VII Comparison of the Reference PSC with the Proposed PSC

Device Structure	**J_{SC} (mA/cm^2)**	**V_{OC} (V)**	**FF (%)**	**PCE (%)**
Glass-base / FTO / $Cd_{0.5}Zn_{0.5}S$ / $MASnI_3$ / $MASnBr_3$ / Au [9]	32.48	0.96	76.40	23.86
ITO/ZnO/$MASnI_3$/ $CuSbS_2$/Ag [32]	33.19	0.876	76.19	22.16
n-TiO_2/i- MASnBr3 /p-NiO [36]	31.88	0.80	84.89	21.66
Glass-base / FTO / AZO / $MASnBr_3$ / $CuSbS_2$ / Au [This Work]	**32.02**	**1.13**	**84.87**	**30.88**

I. Simulation of bottom sub cell

We use the transmitted spectrum from the top sub cell to simulate the bottom sub cell i.e., Crystalline silicon. All the required simulation parameters are taken from [46] and are listed in Table VIII. We have achieved an efficiency of 21.80% by simulating the c-Si standalone cell with the parameters mentioned in Table VIII.

Table VIII: Device parameters for the bottom cell

PARAMETER	**p+ Si**	**p Si**	**n+ Si**
Thickness, µm	10	300	0.5
Relative permittivity, ϵ_r	11.9	11.9	11.9
Bandgap(eV)	1.12	1.12	1.12
Electron Affinity(eV)	4.05	4.05	4.05
Electron Mobility (cm^2/ V.s)	1400	1400	1400
Hole Mobility (cm^2/ V.s)	450	450	450
Conduction Band Density of States/N_c (cm^{-3})	2.8×10^{19}	2.8×10^{19}	2.8×10^{19}
Valence Band Density of States/N_v (cm^{-3})	1.04×10^{19}	1.04×10^{19}	1.04×10^{19}
Donor Concentration, N_d (cm^{-3})	0	0	1.0×10^{20}
Acceptor Concentration, N_a (cm^{-3})	1.0×10^{20}	1.0×10^{16}	0

J. Simulation of the tandem solar cell

We simulate the Tandem solar cell with MASnBr3 – based perovskite solar cell as top cell, c-Si as the bottom cell. While simulating for tandem we optimize few characteristics of top and bottom cell to attain the current matching condition [47]. We have achieved an efficiency of 42.7% for the proposed tandem structure. A JV characteristics curve for the top, bottom and tandem solar cells are given in the Fig. 14.

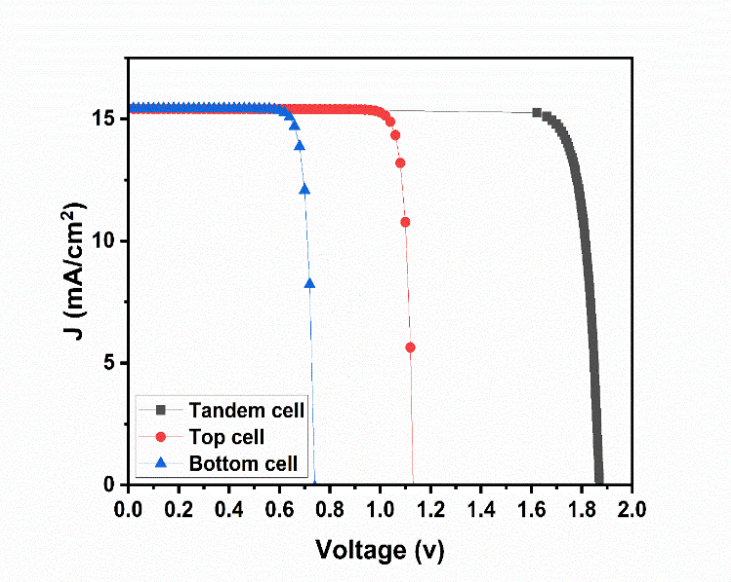

Fig. 14. JV Characteristics

The comparison for the results of the top, bottom and the tandem solar cells are given in the table IX

Table IX Comparison of results for Top, Bottom and Tandem cells

Cell	Voc (v)	Jsc (mA/cm^2)	FF (%)	PCE (%)
MASnBr3	1.13	32.02	84.87	30.88
c-Si	0.74	20.30	85.24	21.80
Tandem	1.87	15.48	85.24	42.70

K. Discussion of proposed structure:

After optimizing the reference PSC by carrying out the simulations as mentioned above, the structure of the proposed TSC is depicted in Fig. 15. The results obtained while optimizing the PSC are recorded in Table X. The PSC with the structure glass base/ FTO/ TiO_2/ $MASnBr_3$/ Spiro-OMeTAD/Au (Fig. 1) had a PCE of 23.30% and from Table X we can see how the PCE increases as the PSC gets optimized. The final optimized PSC with the structure glass base/ FTO/ AZO/ $MASnBr_3$/$CuSbS_2$/Au (Fig. 15) has a PCE of 30.88%. Using this PSC as the top sub cell and c-Si as the bottom cell in TSC we have achieved an efficiency of 42.7%. The improvements in efficiency is shown in the table X.

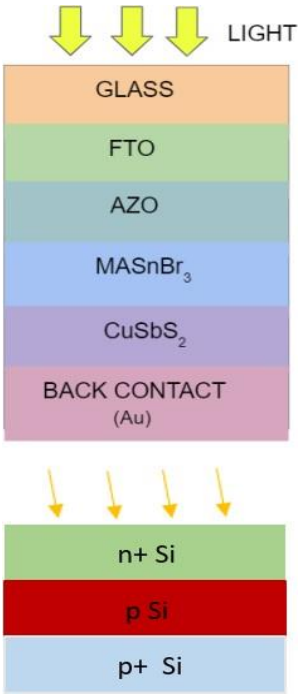

Fig. 15. Proposed tandem solar cell structure

Table X Final results of the proposed PSC

Parameter	Optimum Layer/Value	PCE (%)
ETL materials	AZO	23.45
HTL materials	$CuSbS_2$	24.38
Absorber layer thickness	500 nm	24.38
Absorber layer defect density	1 x 10^{13}	30.70
Thickness of ETL	100 nm	30.70
Thickness of HTL	400 nm	30.81
Band gap of absorber layer [39]	1.33 eV	30.88
Tandem	c-Si as Bottom cell	42.7%

4. Conclusion

Through SCAPS simulation, non-lead PSCs using $MASnBr_3$ perovskite as the absorber layer are studied in this paper. First, the best materials for the ETL and HTL, which are AZO and $CuSbS_2$, respectively, are determined. Following that, the impacts of absorber layer thickness, the density of defect of the absorber layer, band-gap of the Absorber layer, AZO thickness and $CuSbS_2$ thickness on PSC performance are explored. Glass substrate/ FTO/ AZO/ $MASnBr_3$/ $CuSbS_2$ /Au is the PSC's configuration. The optimal absorber layer thickness is 500 nm, according to simulation studies, and a leaner absorber layer will result in bad performance of the cell due to inadequate photon absorption. The simulations revealed an ideal defect density ($1x10^{13}$ cm^{-3}) in the absorber layer, and any defect densities more than that will result in a drop in solar cell efficiency due to the development of more recombination sites. Finally, it was discovered that AZO thickness of 100 nm and $CuSbS_2$ thickness of 400 nm is the most efficient. We also have simulated the Tandem structure using this PSC as the top subcell and c-Si as the bottom sub cell. We have observed a raise the efficiency from 30.88% in single structure to 42.7% in tandem. The findings of this work will aid in the development of non-lead and efficient PSCs, increasing the use of solar energy, along with wave [20], [48], [49] and wind energy [50], [51] as a source of sustainable energy.

5. References

[1] B. J. van Ruijven, E. De Cian, and I. Sue Wing, "Amplification of future energy demand growth due to climate change," *Nat Commun*, vol. 10, no. 1, Dec. 2019, doi: 10.1038/s41467-019-10399-3.

[2] M. Mohan, "Perovskite Photovoltaics," in *Perovskite Photovoltaics*, Elsevier, 2018, pp. 447–480. doi: 10.1016/B978-0-12-812915-9.00014-9.

[3] A. K. Jena, A. Kulkarni, and T. Miyasaka, "Halide Perovskite Photovoltaics: Background, Status, and Future Prospects," *Chem Rev*, vol. 119, no. 5, pp. 3036–3103, Mar. 2019, doi: 10.1021/acs.chemrev.8b00539.

[4] R. Kour *et al.*, "Potential Substitutes for Replacement of Lead in Perovskite Solar Cells: A Review," *Global Challenges*, vol. 3, no. 11, p. 1900050, Nov. 2019, doi: 10.1002/gch2.201900050.

[5] T.-B. Song, T. Yokoyama, S. Aramaki, and M. G. Kanatzidis, "Performance Enhancement of Lead-Free Tin-Based Perovskite Solar Cells with Reducing Atmosphere-Assisted Dispersible Additive," *ACS Energy Lett*, vol. 2, no. 4, pp. 897–903, Apr. 2017, doi: 10.1021/acsenergylett.7b00171.

[6] M. A. Green, A. Ho-Baillie, and H. J. Snaith, "The emergence of perovskite solar cells," *Nat Photonics*, vol. 8, no. 7, pp. 506–514, Jul. 2014, doi: 10.1038/nphoton.2014.134.

[7] A. Kojima, K. Teshima, Y. Shirai, and T. Miyasaka, "Organometal Halide Perovskites as Visible-Light Sensitizers for Photovoltaic Cells," *J Am Chem Soc*, vol. 131, no. 17, pp. 6050–6051, May 2009, doi: 10.1021/ja809598r.

[8] H. Xu, H. Yuan, J. Duan, Y. Zhao, Z. Jiao, and Q. Tang, "Lead-free CH3NH3SnBr3-xIx perovskite quantum dots for mesoscopic solar cell applications," *Electrochim Acta*, vol. 282, pp. 807–812, Aug. 2018, doi: 10.1016/j.electacta.2018.05.143.

[9] Y. Gan *et al.*, "Numerical Investigation Energy Conversion Performance of Tin-Based Perovskite Solar Cells Using Cell Capacitance Simulator," *Energies (Basel)*, vol. 13, no. 22, p. 5907, Nov. 2020, doi: 10.3390/en13225907.

[10] L. L. Yan, C. Han, B. Shi, Y. Zhao, and X. D. Zhang, "A review on the crystalline silicon bottom cell for monolithic perovskite/silicon tandem solar cells," *Mater Today Nano*, vol. 7, p. 100045, Aug. 2019, doi: 10.1016/j.mtnano.2019.100045.

[11] Z. J. Yu, J. V. Carpenter, and Z. C. Holman, "Techno-economic viability of silicon-based tandem photovoltaic modules in the United States," *Nat Energy*, vol. 3, no. 9, pp. 747–753, Jul. 2018, doi: 10.1038/s41560-018-0201-5.

[12] S. Rühle, "Tabulated values of the Shockley–Queisser limit for single junction solar cells," *Solar Energy*, vol. 130, pp. 139–147, Jun. 2016, doi: 10.1016/j.solener.2016.02.015.

[13] M. Burgelman, P. Nollet, and S. Degrave, "Modelling polycrystalline semiconductor solar cells," *Thin Solid Films*, vol. 361–362, pp. 527–532, Feb. 2000, doi: 10.1016/S0040-6090(99)00825-1.

[14] F. Baig, Y. H. Khattak, B. Marí, S. Beg, A. Ahmed, and K. Khan, "Efficiency Enhancement of CH3NH3SnI3 Solar Cells by Device Modeling," *J Electron Mater*, vol. 47, no. 9, pp. 5275–5282, Sep. 2018, doi: 10.1007/s11664-018-6406-3.

[15] F. Azri, A. Meftah, N. Sengouga, and A. Meftah, "Electron and hole transport layers optimization by numerical simulation of a perovskite solar cell," *Solar Energy*, vol. 181, pp. 372–378, Mar. 2019, doi: 10.1016/j.solener.2019.02.017.

[16] T. Minemoto and M. Murata, "Impact of work function of back contact of perovskite solar cells without hole transport material analyzed by device simulation," *Current Applied Physics*, vol. 14, no. 11, pp. 1428–1433, Nov. 2014, doi: 10.1016/j.cap.2014.08.002.

[17] R. Teimouri and R. Mohammadpour, "Potential application of CuSbS 2 as the hole transport material in perovskite solar cell: A simulation study," *Superlattices Microstruct*, vol. 118, pp. 116–122, Jun. 2018, doi: 10.1016/j.spmi.2018.03.079.

[18] L. Lin, L. Jiang, P. Li, B. Fan, and Y. Qiu, "A modeled perovskite solar cell structure with a Cu2O hole-transporting layer enabling over 20% efficiency by low-cost low-temperature processing," *Journal of Physics and Chemistry of Solids*, vol. 124, pp. 205–211, Jan. 2019, doi: 10.1016/j.jpcs.2018.09.024.

[19] N. Lakhdar and A. Hima, "Electron transport material effect on performance of perovskite solar cells based on CH3NH3GeI3," *Opt Mater (Amst)*, vol. 99, p. 109517, Jan. 2020, doi: 10.1016/j.optmat.2019.109517.

[20] L. Lin, L. Jiang, Y. Qiu, and B. Fan, "Analysis of Sb2Se3/CdS based photovoltaic cell: A numerical simulation approach," *Journal of Physics and Chemistry of Solids*, vol. 122, pp. 19–24, Nov. 2018, doi: 10.1016/j.jpcs.2018.05.045.

[21] H.-K. Lin, J.-X. Li, H.-C. Wang, Y.-W. Su, K.-H. Wu, and K.-H. Wei, "Dual nanocomposite carrier transport layers enhance the efficiency of planar perovskite photovoltaics," *RSC Adv*, vol. 8, no. 23, pp. 12526–12534, 2018, doi: 10.1039/C8RA01532E.

[22] P. Altermatt, "Numerical Simulation of Crystalline Silicon Solar Cells," in *Photovoltaic Solar Energy*, Chichester, UK: John Wiley & Sons, Ltd, 2017, pp. 150–159. doi: 10.1002/9781118927496.ch15.

[23] J. Verschraegen and M. Burgelman, "Numerical modeling of intra-band tunneling for heterojunction solar cells in scaps," *Thin Solid Films*, vol. 515, no. 15, pp. 6276–6279, May 2007, doi: 10.1016/j.tsf.2006.12.049.

[24] K. Kim *et al.*, "Simulations of chalcopyrite/c-Si tandem cells using SCAPS-1D," *Solar Energy*, vol. 145, pp. 52–58, Mar. 2017, doi: 10.1016/j.solener.2017.01.031.

[25] U. Mandadapu, "Simulation and Analysis of Lead based Perovskite Solar Cell using SCAPS-1D," *Indian J Sci Technol*, vol. 10, no. 1, pp. 1–8, Jan. 2017, doi: 10.17485/ijst/2017/v11i10/110721.

[26] I. Spanopoulos *et al.*, "Unraveling the Chemical Nature of the 3D 'Hollow' Hybrid Halide Perovskites," *J Am Chem Soc*, vol. 140, no. 17, pp. 5728–5742, May 2018, doi: 10.1021/jacs.8b01034.

[27] M. Szafrański and A. Katrusiak, "Photovoltaic Hybrid Perovskites under Pressure," *J Phys Chem Lett*, vol. 8, no. 11, pp. 2496–2506, Jun. 2017, doi: 10.1021/acs.jpclett.7b00520.

[28] A. Shukla, V. K. Sharma, S. K. Gupta, and A. S. Verma, "Computational determination of the physical-thermoelectric parameters of tin-based organomatallic halide perovskites (CH3NH3SnX3, X = Br and I): Emerging materials for optoelectronic devices," *Mater Chem Phys*, vol. 253, p. 123389, Oct. 2020, doi: 10.1016/j.matchemphys.2020.123389.

[29] J. Jiang, C. K. Onwudinanti, R. A. Hatton, P. A. Bobbert, and S. Tao, "Stabilizing Lead-Free All-Inorganic Tin Halide Perovskites by Ion Exchange," *The Journal of Physical Chemistry C*, vol. 122, no. 31, pp. 17660–17667, Aug. 2018, doi: 10.1021/acs.jpcc.8b04013.

[30] F. Hao, C. C. Stoumpos, R. P. H. Chang, and M. G. Kanatzidis, "Anomalous Band Gap Behavior in Mixed Sn and Pb Perovskites Enables Broadening of Absorption Spectrum in Solar Cells," *J Am Chem Soc*, vol. 136, no. 22, pp. 8094–8099, Jun. 2014, doi: 10.1021/ja5033259.

[31] F. Hao *et al.*, "Solvent-Mediated Crystallization of CH 3 NH 3 SnI 3 Films for Heterojunction Depleted Perovskite Solar Cells," *J Am Chem Soc*, vol. 137, no. 35, pp. 11445–11452, Sep. 2015, doi: 10.1021/jacs.5b06658.

[32] S. Bhattarai *et al.*, "Investigation of Carrier Transport Materials for Performance Assessment of Lead-Free Perovskite Solar Cells," *IEEE Trans Electron Devices*, vol. 69, no. 6, pp. 3217–3224, Jun. 2022, doi: 10.1109/TED.2022.3165516.

[33] S. Gupta, T. Bendikov, G. Hodes, and D. Cahen, "CsSnBr 3 , A Lead-Free Halide Perovskite for Long-Term Solar Cell Application: Insights on SnF 2 Addition," *ACS Energy Lett*, vol. 1, no. 5, pp. 1028–1033, Nov. 2016, doi: 10.1021/acsenergylett.6b00402.

[34] L. K. Ono and Y. Qi, "Surface and Interface Aspects of Organometal Halide Perovskite Materials and Solar Cells," *J Phys Chem Lett*, vol. 7, no. 22, pp. 4764–4794, Nov. 2016, doi: 10.1021/acs.jpclett.6b01951.

[35] X. Liu *et al.*, "Improved efficiency and stability of Pb–Sn binary perovskite solar cells by Cs substitution," *J Mater Chem A Mater*, vol. 4, no. 46, pp. 17939–17945, 2016, doi: 10.1039/C6TA07712A.

[36] Md. Samiul Islam *et al.*, "Defect Study and Modelling of SnX3-Based Perovskite Solar Cells with SCAPS-1D," *Nanomaterials*, vol. 11, no. 5, p. 1218, May 2021, doi: 10.3390/nano11051218.

[37] K. Tanaka, T. Minemoto, and H. Takakura, "Analysis of heterointerface recombination by Zn1−xMgxO for window layer of Cu(In,Ga)Se2 solar cells," *Solar Energy*, vol. 83, no. 4, pp. 477–479, Apr. 2009, doi: 10.1016/j.solener.2008.09.003.

[38] M. Turcu and U. Rau, "Fermi level pinning at CdS/Cu(In,Ga)(Se,S)2 interfaces: effect of chalcopyrite alloy composition," *Journal of Physics and Chemistry of Solids*, vol. 64, no. 9–10, pp. 1591–1595, Sep. 2003, doi: 10.1016/S0022-3697(03)00137-9.

[39] T. Minemoto and M. Murata, "Theoretical analysis on effect of band offsets in perovskite solar cells," *Solar Energy Materials and Solar Cells*, vol. 133, pp. 8–14, Feb. 2015, doi: 10.1016/j.solmat.2014.10.036.

[40] H.-J. Du, W.-C. Wang, and J.-Z. Zhu, "Device simulation of lead-free CH 3 NH 3 SnI 3 perovskite solar cells with high efficiency," *Chinese Physics B*, vol. 25, no. 10, p. 108802, Oct. 2016, doi: 10.1088/1674-1056/25/10/108802.

[41] V. M. Le Corre *et al.*, "Revealing Charge Carrier Mobility and Defect Densities in Metal Halide Perovskites via Space-Charge-Limited Current Measurements," *ACS Energy Lett*, vol. 6, no. 3, pp. 1087–1094, Mar. 2021, doi: 10.1021/acsenergylett.0c02599.

[42] N. Devi, K. A. Parrey, A. Aziz, and S. Datta, "Numerical simulations of perovskite thin-film solar cells using a CdS hole blocking layer," *Journal of Vacuum Science & Technology B*, vol. 36, no. 4, p. 04G105, Jul. 2018, doi: 10.1116/1.5026163.

[43] K. Tan, P. Lin, G. Wang, Y. Liu, Z. Xu, and Y. Lin, "Controllable design of solid-state perovskite solar cells

by SCAPS device simulation," *Solid State Electron*, vol. 126, pp. 75–80, Dec. 2016, doi: 10.1016/j.sse.2016.09.012.

[44] A. Pisanu *et al.*, "Exploring the Limits of Three-Dimensional Perovskites: The Case of FAPb 1– *x* Sn *x* Br 3," *ACS Energy Lett*, vol. 3, no. 6, pp. 1353–1359, Jun. 2018, doi: 10.1021/acsenergylett.8b00615.

[45] I. Spanopoulos *et al.*, "Unraveling the Chemical Nature of the 3D 'Hollow' Hybrid Halide Perovskites," *J Am Chem Soc*, vol. 140, no. 17, pp. 5728–5742, May 2018, doi: 10.1021/jacs.8b01034.

[46] M. T. Islam *et al.*, "Investigation of CsSn0.5Ge0.5I3-on-Si Tandem Solar Device Utilizing SCAPS Simulation," *IEEE Trans Electron Devices*, vol. 68, no. 2, pp. 618–625, Feb. 2021, doi: 10.1109/TED.2020.3045383.

[47] C. Ulbrich *et al.*, "Matching of Silicon Thin-Film Tandem Solar Cells for Maximum Power Output," *International Journal of Photoenergy*, vol. 2013, pp. 1–7, 2013, doi: 10.1155/2013/314097.

[48] K. Guiberteau, J. Lee, Y. Liu, Y. Dou, and T. A. Kozman, "Wave Energy Converters and Design Considerations for Gulf of Mexico," *Distributed Generation & Alternative Energy Journal*, vol. 30, no. 4, pp. 55–76, Sep. 2015, doi: 10.1080/21563306.2015.11667613.

[49] J. Pastor and Y. Liu, "Hydrokinetic Energy: Overview and it's Renewable Energy Potential for the Gulf of Mexico," in *2012 IEEE Green Technologies Conference*, IEEE, Apr. 2012, pp. 1–3. doi: 10.1109/GREEN.2012.6200995.

[50] W. Zheng, Y. W. Liu, X. G. Hu, and C. F. Zhang, "Novel nanosized adsorbing sulfur composite cathode materials for the advanced secondary lithium batteries," *Electrochim Acta*, vol. 51, no. 7, pp. 1330–1335, Jan. 2006, doi: 10.1016/j.electacta.2005.06.021.

[51] S. J. Chu and Y. Liu, "Prospects of Wind Power and Wind Energy in Louisiana," in *2011 IEEE Green Technologies Conference (IEEE-Green)*, IEEE, Apr. 2011, pp. 1–6. doi: 10.1109/GREEN.2011.5754871.